

Article

Shielded Capacitive Power Transfer (S-CPT) without Secondary Side Inductors

Suziana Ahmad ^{1,2}, Aam Muharam ³, Reiji Hattori ^{1,*}, Anyu Uezu ¹ and Tarek M. Mostafa ⁴

¹ Interdisciplinary Graduate School of Engineering Sciences, Kyushu University, Fukuoka 816-8580, Japan; suziana@utem.edu.my (S.A.); uezu.anyu.340@s.kyushu-u.ac.jp (A.U.)

² Faculty of Electrical and Electronic Engineering Technology, Universiti Teknikal Malaysia Melaka, Malacca 76100, Malaysia

³ Research Centre for Electrical Power and Mechatronics, Indonesian Institute of Sciences, Bandung 40135, Indonesia; aam.muhamam@lipi.go.id

⁴ CEMSE Division, King Abdullah University of Science and Technology (KAUST), Thuwal 23955-6900, Saudi Arabia; tarek.mostafa@kaust.edu.sa

* Correspondence: hattori@gic.kyushu-u.ac.jp; Tel.: +81-92-583-7887

Abstract: In this study, we propose a four-plate structure with two shielding plates to produce shielded capacitive power transfer (S-CPT) at an operating frequency of 6.78 MHz for a 10 W system. By eliminating the inductors at the secondary side to form an asymmetrical topology, an S-CPT system was developed with a class-E power amplifier. Using MATLAB software, analysis was performed to obtain the parameters in the S-CPT system regarding resonance and impedance matching, and the proposed coupler structure was investigated through electric field simulation. The shield plate voltage stability was also investigated by analysing both the simulation and hardware experiment results. A prototype of S-CPT was established to validate the analysis results and to demonstrate the voltage at the shield plate of the proposed coupler structure. The experimental results are in good agreement with the simulation results. The proposed S-CPT exhibits an AC–AC efficiency of 84%, with a 56% voltage ground stability reduction because of implementing a balun.

Keywords: wireless power transfer; capacitive; class-E inverter

Citation: Ahmad, S.; Muharam, A.; Hattori, R.; Uezu, A.; Mostafa, T.M. Shielded Capacitive Power Transfer (S-CPT) without Secondary Side Inductors. *Energies* **2021**, *14*, 4590. <https://doi.org/10.3390/en14154590>

Academic Editor: ByoungHee Lee

Received: 8 June 2021

Accepted: 27 July 2021

Published: 29 July 2021

Publisher's Note: MDPI stays neutral with regard to jurisdictional claims in published maps and institutional affiliations.



Copyright: © 2021 by the authors. Licensee MDPI, Basel, Switzerland. This article is an open access article distributed under the terms and conditions of the Creative Commons Attribution (CC BY) license (<http://creativecommons.org/licenses/by/4.0/>).

1. Introduction

Capacitive power transfer (CPT) has gained interest amongst researchers in wireless power transfer technology. In the CPT system, power is transferred between plates through an electric field (EF). Recently, CPT technology has become an interesting topic in several applications, such as electric vehicle charging systems [1–4], drones [5,6], and rotary operations [7–10].

CPT comprises a DC supply, an inverter, a capacitive coupler, and a load. A resonant inverter, such as a class-E inverter [4,11–13], is used to resonate the AC supply with the designated operating frequency of a CPT system. A major component of the CPT system is the coupler, which acts as an interface and transfers the electric field between the primary and secondary components. Furthermore, the coupler structure has been introduced in different designs of CPT systems, such as four-plate structure [1,14–16], six-plate structure [17], and four-plate structure with a shield plate [18–20]. The coupler is arranged either vertically or horizontally depending on the designated application. Compared with the four-plate structure, a six-plate coupler with a parallel arrangement can reduce the EF emission in CPT systems [17,19]. Therefore, the shielding plate system can enhance the safety of CPT. However, misalignment between the six-plate structure increases the EF emission and decreases CPT efficiency [17]. Furthermore, the four-plate structure minimises the EF emission by using a grounding connection to the plate [15].

S-CPT, comprising four coupler plates with shield plates, has been introduced [18,20,21]. Figure 1 shows an S-CPT system design in which the coupler plates and shield plates are arranged in parallel. Both the primary and secondary sides have two coupler plates and a shield plate. The principal advantage is that the shield plates minimise EF emission [19].

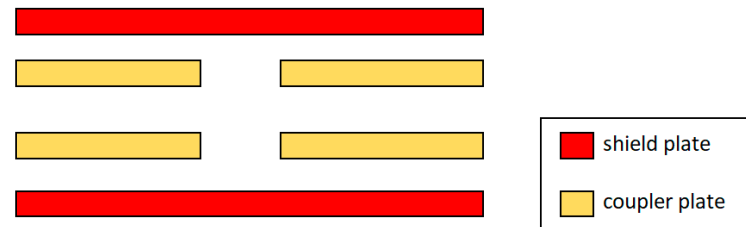


Figure 1. Four-plate couplers with shielded plates.

This study developed an S-CPT system with a class-E power amplifier that has an operating frequency of 6.78 MHz by eliminating the inductor at the secondary side. An analytical method was used to obtain the parameters in S-CPT by considering the resonance condition and impedance matching condition. The coupler was designed, and the EF emission was studied. The S-CPT system was connected to a class-E power amplifier. To investigate the voltage at the shield plates, S-CPT systems (with and without a balun) were constructed in both the simulation and experiment.

2. S-CPT System

A generalised circuit of S-CPT can be formed into symmetrical and asymmetrical topologies in which the symmetrical topology has advantages in terms of the stability of the load changing, whereas the asymmetrical topology has the advantage of being lightweight at the receiver side [20]. Symmetrical and asymmetrical S-CPTs systems must be designed in resonance and matching conditions as the major design requirements. In the resonance condition, the S-CPT system has a total impedance of the resistive part with zero reactance part, with a total admittance equal to 0.01 in the matching condition for transferring maximum power [20].

Figure 2a shows the S-CPT system with an inductor at both the primary and secondary sides. Eliminating the inductor on the secondary side transforms the symmetrical circuit into an asymmetrical topology. The inductor's internal series resistance affects the total current in S-CPT in terms of loss and efficiency [20]. Eliminating the secondary circuit resulted in a lightweight and compact S-CPT design. Therefore, for applications such as drones and robots that must be lightweight, the symmetrical topology has a potential solution for wireless power transfer. Accordingly, this study focused on the asymmetrical configuration and investigated the ground voltage stability and EF emission.

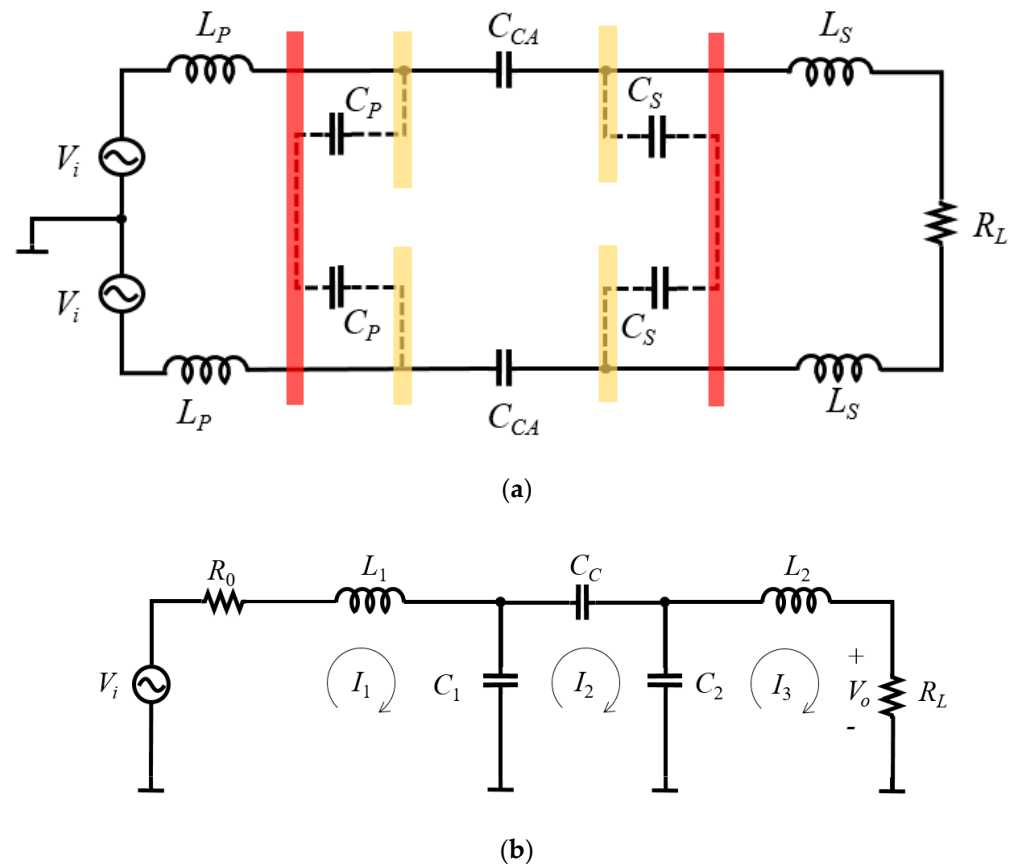


Figure 2. S-CPT diagram. (a) Symmetrical S-CPT circuit. (b) Equivalent circuit of the symmetrical S-CPT circuit.

Figure 2a shows the component arrangement in the S-CPT system, in which the capacitance represents the six-coupler plate structure with a voltage input V_i and load resistance R_L . The capacitance of the S-CPT structure is modelled by the primary coupler to the secondary coupler and the parasitic capacitance between the coupler and shielding plate only. Other parasitic characteristics were excluded—such as cross-coupling capacitance, edge side-to-side capacitance, and shield plate to ground capacitance—from the analysis. Therefore, Figure 2a presents the capacitance model, with C_c as the capacitance between the coupler plate and at the primary and secondary sides. The parasitic capacitance at the primary C_P is the capacitance between the coupler plate and shielding plate. The parasitic capacitance C_S is the capacitance between the coupler and the shielding plate at the secondary part. The inductor L_P is placed on the primary side, and the load R_L is located in the secondary part. On the secondary side, the inductor L_S is connected to the load. The S-CPT circuit diagram can be simplified into an equivalent circuit [20], as shown in Figure 2b, by mirroring the x -axis structure shown in Figure 2a.

Figure 2b shows the equivalent circuit of S-CPT to represent the symmetrical circuit, as shown in Figure 2a, where R_0 is the internal characteristic of the power source. Figure 3a shows the coupler structure of S-CPT with four coupler and two shield plates, and Figure 3b shows the equivalent circuit of the coupler. In Figure 3b, the capacitance C_1 is denoted by the total series capacitance C_P on the primary side.

The secondary capacitance, C_2 , equals the total series of inductor C_S . Obtaining the capacitance parameters shown in Figure 3b involves using the two-port network method, assuming that both circuits in Figure 3a,b have the same value as the ABCD transmission parameter matrix as in Equation (1) and $s = j * \omega$, in which ω is the angular frequency. Solving both circuits in Figure 3 using a MATLAB simulation with the same parameters

of the ABCD matrix implies Equation (2) provides the coupling capacitance C_c , whilst Equations (3) and (4) provide the primary and secondary capacitances, respectively.

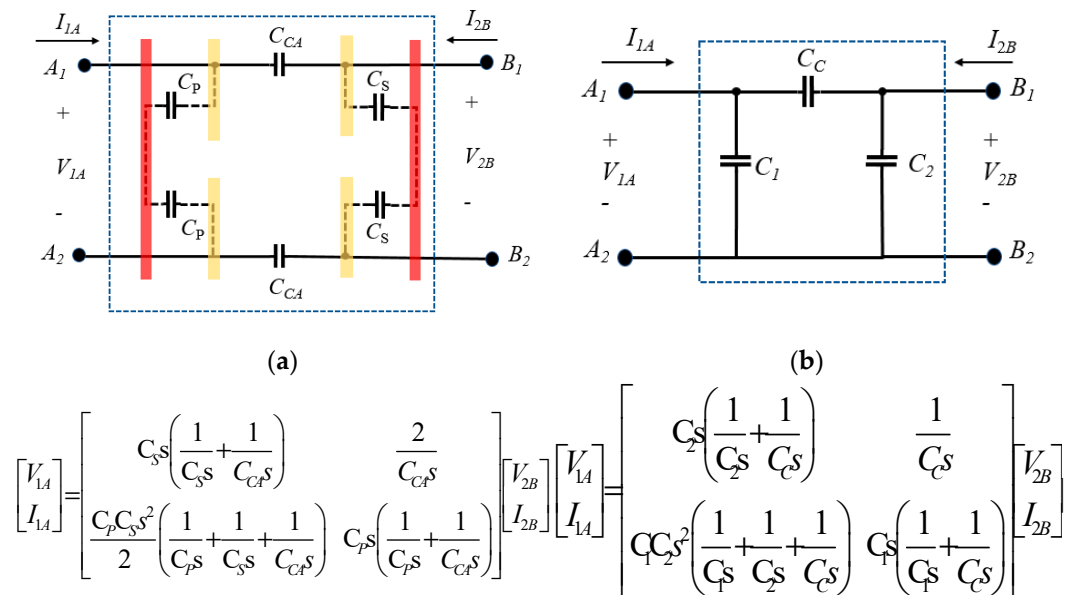


Figure 3. S-CPT coupler. (a) Coupler with the capacitance model. (b) Equivalent circuit of the coupler.

$$\begin{bmatrix} V_{1A} \\ I_{1A} \end{bmatrix} = \begin{bmatrix} A & B \\ C & D \end{bmatrix} \begin{bmatrix} V_{2B} \\ I_{2B} \end{bmatrix} \tag{1}$$

$$C_c = \frac{C_{CA}}{2} \tag{2}$$

$$C_1 = \frac{C_P}{2} \tag{3}$$

$$C_2 = \frac{C_S}{2} \tag{4}$$

When the inductor at the primary L_1 is inserted at the circuit, as shown in Figure 2b, the inductor in Figure 2a will become half of L_1 because the total inductors for both circuits are the same. In the simplification expression, $L_P = 0.5 \times L_1$, and $L_S = 0.5 \times L_2$. On the secondary side, the secondary capacitance C_2 and secondary inductor L_2 are denoted by the total series capacitance C_2 and double value of the secondary inductor L_S . Therefore, the equivalent circuit shown in Figure 2b is formed from Figure 2a based on the relationship between the parameters. In Figure 2b, the Kirchhoff voltage law (KVL) represents I_1 , I_2 , and I_3 . Using the same analysis as described in [20], the KVL equations of I_1 , I_2 , and I_3 can be obtained as in Equation (5). Solving the expressions of I_1 , I_2 , and I_3 involves using linear methods with a variable method, and the current to voltage equation, I_1/V_i , can be obtained as in Equation (6).

$$\begin{bmatrix} \left(j\omega L_1 + \frac{1}{j\omega C_1} + R_0\right) & -\frac{1}{j\omega C_1} & 0 \\ -\frac{1}{j\omega C_1} & \left(\frac{1}{j\omega C_1} + \frac{1}{j\omega C_c} + \frac{1}{j\omega C_2}\right) & -\frac{1}{j\omega C_2} \\ 0 & -\frac{1}{j\omega C_2} & \left(j\omega L_2 + \frac{1}{j\omega C_2} + R_L\right) \end{bmatrix} \begin{bmatrix} I_1 \\ I_2 \\ I_3 \end{bmatrix} = \begin{bmatrix} V_i \\ 0 \\ 0 \end{bmatrix} \quad (5)$$

$$\frac{I_1}{V_i} = \frac{j\omega C \{-\omega^2 MCL_2 + N + j\omega MCR_L\}}{\left[\omega^4 MC^2 L_1 L_2 + \omega^2 C \{MCR_0 R_L + NL_1 + QL_2\} + T\right] - j\left[\omega^3 MC^2 (L_1 R_L + L_2 R_0) - \omega C \{QR_L + NR_0\}\right]} \quad (6)$$

where $\begin{bmatrix} M \\ N \\ Q \\ T \end{bmatrix} \equiv \begin{bmatrix} ar^2 \\ (ar-1) \\ (a-1)r^2 \\ (ar-r-1) \end{bmatrix}$.

The ratio of the secondary capacitor C_2 to the primary capacitor C_1 , $r = C_2/C_1$, and the relationship between the coupling capacitance and the shield coupler is $a = 1 + C/C_c + 1/r$.

The value of the operating frequency f and angular frequency $\omega = 2\pi f$. The value C is equal to the primary capacitance, $C = C_1$.

Two approximations have been used to analyse and simplify the S-CPT circuit. First, total impedance can be calculated if a resonance condition occurs in the circuit with the assumption that all components in the S-CPT system are modelled by the single impedance Z_T . Second, the match impedance condition in which the impedance at the input is equal to the output impedance by considering that the input power supply device has a match impedance load to S-CPT. Therefore, the equivalent circuit in Figure 2b can be simplified into a series circuit, as shown in Figure 4, in which it is arranged with total impedance Z_T . The circuit consists of the total impedance Z_T as the output impedance, voltage source V_i with an operating frequency f , and internal series resistance R_0 as the input load.

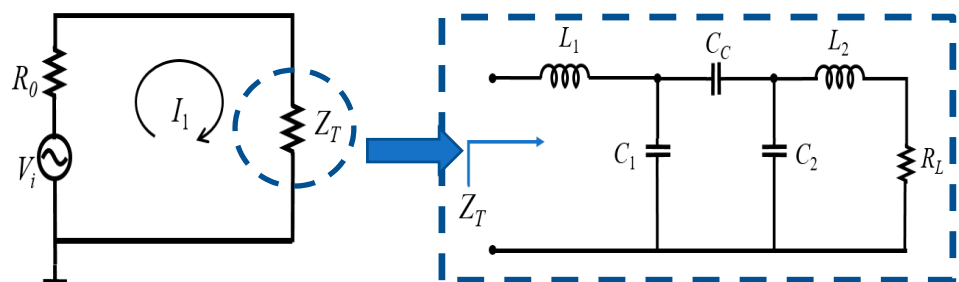


Figure 4. A simplified circuit of the S-CPT circuit.

Figure 4 shows the simplified circuit model for the analysis process, assuming that the circuit is in the resonance and match impedance conditions. In the resonance condition, the total impedance Z_T is given by the resistive part with zero reactance. In the match impedance circuit, the impedance Z_T is equal to the input impedance R_0 to transfer the maximum power. Therefore, the I_1/V_i shown in Equation (6) is solved in the resonance condition to deduce the inductor value by taking the total reactance in the circuit to be equal to zero, in which the total circuit impedance is contributed by the resistive part with no imaginary part. In the match impedance condition, the magnitude of current to voltage, $|I_1/V_i|$, is equal to 1/100 or 0.01 [19] by taking both the input internal resistance and

output load impedance equal to 50 Ω, in which the total impedance is equal to 100 Ω. Therefore, the S-CPT system in this analysis considers a 50 Ω impedance match between the supply load and S-CPT load.

In the symmetrical circuit, the primary inductor L_1 is equal to the secondary inductor L_2 , whereas the shield plate capacitance at both the primary and secondary parts are the same, $C = C_1$, with the ratio of the primary capacitance to the secondary capacitance $r = 1$. Therefore, the deduced inductor value that uses Equation (2) with the resonance condition is obtained in Equation (7). A MATLAB simulation was used to perform the calculation process.

$$L_1 = L_2 = \frac{(C + C_c)}{(C^2 + 2C_c C)} \omega^2 \pm \frac{(C + C_c)}{(C^2 + 2C_c C)} \omega^2 \sqrt{\frac{-(C^2 R_l \omega + 2C_c C R_l \omega + C_c)(C^2 R_l \omega + 2C_c C R_l \omega - C_c)}{(C^2 + 2C_c C) \omega^2}} \quad (7)$$

Equation (7) shows the relationship between the inductor and other parameters, which shows that the symmetrical circuit produces three possible values of inductors in which it can be formed into three topologies of symmetrical S-CPT. In reference to Equation (7), one of the S-CPT systems has no relationship between the R_L load and the inductor value, whilst the other two systems have a relationship between the inductor and the R_L load. Based on the symmetrical S-CPT analysis, the S-CPT topologies are formed into asymmetrical topologies, as shown in Figure 5.

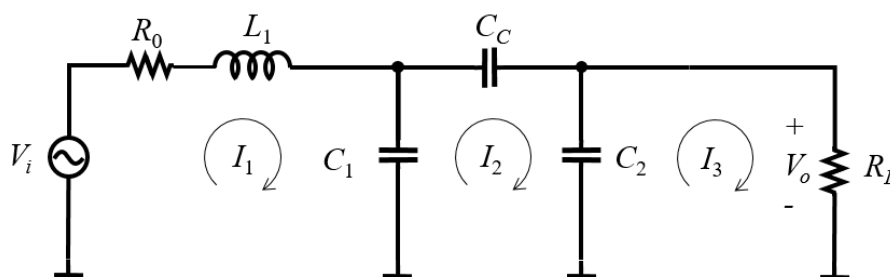


Figure 5. An equivalent of asymmetrical S-CPT.

Figure 5 shows asymmetrical S-CPT in which the primary inductor L_1 is arranged with the shield plate capacitance C_1 and C_2 and the coupling capacitance C_c with no inductance at the secondary side. Therefore, the primary inductor L_1 can be expressed in Equation (6) by having the secondary inductor L_2 equal to zero and the obtained equation calculated as in Equation (8).

$$L_1 = \frac{[(C_2 + C_c)(C_1 C_2 + C_1 C_c + C_2 C_c) R_L^2 \omega^3 + (C_1 + C_c) \omega]}{[\omega^3 (C_1 + C_c)^2 + R_L^2 \omega^5 (C_1 C_2 + C_1 C_c + C_2 C_c)^2]} \quad (8)$$

Equation (8) shows the relationship between the primary inductor L_1 and other parameters in the S-CPT system. Further analysis was performed to calculate the inductor value in both symmetrical and asymmetrical topologies using the analysis test parameters listed in Table 1. Moreover, these topologies were tested in a simulation to study the performance of the resonance and matching impedance conditions.

Table 1. Analysis test parameters of the S-CPT system.

Parameter	Symbol	Analysis S-CPT
Operating frequency	f	6.78 MHz
Coupling capacitance	C_c	5 pF
Shield-coupling primary	C_1	6 pF
Shield-coupling secondary	C_2	6 pF
Load resistance	R_L	50 Ω

Table 1 lists the analysis test parameters for both the symmetrical and asymmetrical circuits. An operating frequency of 6.78 MHz is selected with a 50 Ω load. The S-CPT system uses an operating frequency of 6.78 MHz, which is the lowest value used for the industrial, scientific, and medical bands for MHz wireless power transfer. The International Telecommunication Union Radio recommends an operating frequency of 6.78 MHz because it has little or no negative effect on other licensed bands [19]. The primary capacitance C_1 and the secondary capacitance C_2 with the ratio $r = 1$ is selected in the analysis study. The relationship between the coupling capacitance and the shield coupler is given by $a = 3.2$.

Based on the analysis of the calculation process in the MATLAB simulation, the inductor value was obtained. In symmetrical S-CPT, Equation (3) was used to calculate the inductor's value both at the primary and secondary sides as 34.46 μH , 63.14 μH , and 91.82 μH . Symmetrical S-CPT has three different values of inductor for the three topologies of symmetrical S-CPT, as discussed in the analysis section. In the asymmetrical S-CPT analysis, Equation (8) was used to calculate an inductor value at the primary side with zero inductance value at the secondary side. Table 2 presents the results of the analyses.

Table 2. Analysis results on the S-CPT systems.

Parameter	Symbol	Symmetrical S-CPT			Asymmetrical S-CPT
		A	B	C	
Primary inductor	L_1	34.46 μH	63.14 μH	91.82 μH	50.10 μH
Secondary inductor	L_2	34.46 μH	63.14 μH	91.82 μH	0

Table 2 shows the calculated results obtained from the MATLAB simulation. The analysis parts with calculated inductor values show that S-CPT can be formed into symmetrical and asymmetrical topologies. Symmetrical S-CPT has three topologies, considering the three different inductors, whereas asymmetrical S-CPT has an inductor value at the primary but no inductor at the secondary.

Based on the findings of the analysis, I_1/V_i , as in Equation (6), was used to further analyse the symmetrical and asymmetrical S-CPT with the calculated values and parameters in Table 1. The magnitude $|I_1/V_i|$ for S-CPT was simulated in MATLAB software using the value of inductors, as shown in Table 2. The simulation of $|I_1/V_i|$ was performed to investigate the resonance and matching impedance conditions of the S-CPT system in both symmetrical and asymmetrical topologies. Figure 6 plots the results obtained based on the simulation.

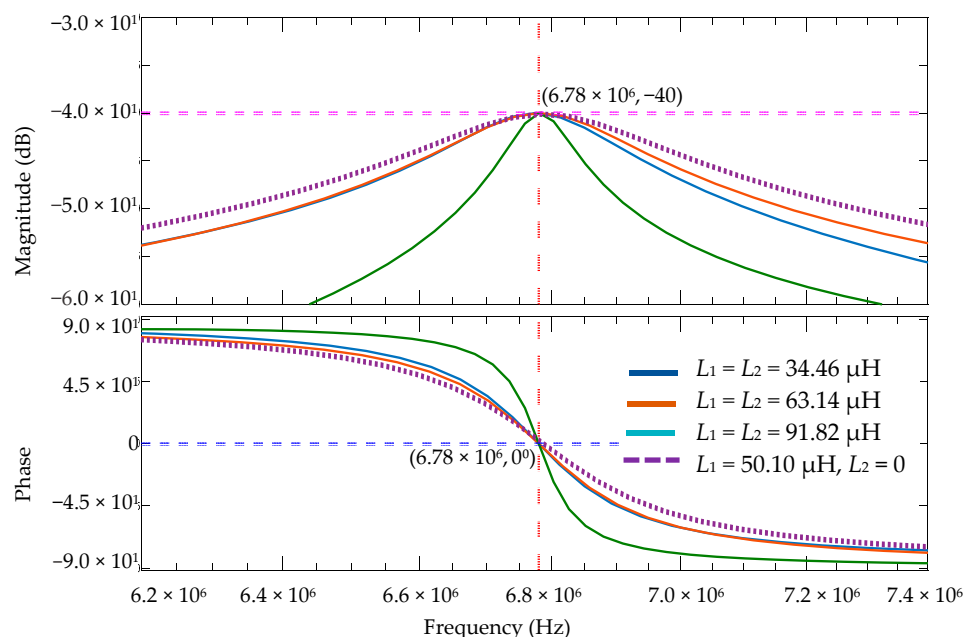


Figure 6. $|I_1/V_i|$ value in magnitude and phase for both symmetrical and asymmetrical topologies.

Figure 6 shows the magnitude and phase of $\mu\text{H } I_1/V_i$ for symmetrical S-CPT ($L_1 = L_2 = 34.46 \mu\text{H}$, $63.14 \mu\text{H}$, $91.82 \mu\text{H}$) and asymmetrical S-CPT ($L_1 = 50.10 \mu\text{H}$, $L_2 = 0$). A straight line plotted in the graph at the x -axis of 6.78 MHz shows the operating frequency. In the phase part, all the topologies have the same value of 0° at 6.78 MHz. In the resonance condition, the current to magnitude $|I_1/V_i|$ is 0° in phase owing to the total impedance of S-CPT, and Z_T has a resistive part and zero reactance. Therefore, the line plotted along the y -axis at the 0° phase serves as a reference to the obtained result. The result shows that both symmetrical and asymmetrical topologies are under the resonance condition by the plotting graph passing through the 0° phase at 6.78 MHz.

The S-CPT topology is under the match impedance condition at the magnitude of $|I_1/V_i| = 0.01$ [19,20] or -40 dB, as discussed in the analysis section by referring to Figure 4, in which S-CPT has a match impedance between the input and output impedances to maximise the power transfer. Figure 6 shows the magnitude of both the symmetrical and asymmetrical S-CPT topologies approaching -40 dB at 6.78 MHz. In the match impedance condition, the total impedance Z_T equals the internal series resistance of the power supply R_0 . Symmetrical S-CPT B ($L_1 = L_2 = 63.14 \mu\text{H}$), as shown in Table 2, approaches -40 dB at 6.78 MHz or in the match impedance when the load equals 30 k Ω because the inductor has no relationship with the load resistance R_L , as reflected in Equation (2). Therefore, S-CPT B has an effective load of 30 k Ω to obtain the match impedance condition. S-CPT A and S-CPT C have an effective load of 50Ω , and asymmetrical S-CPT has an effective load of 250Ω . The effect of the load on asymmetrical S-CPT was studied and the results of the magnitude and phase $|I_1/V_i|$ are presented in Figure 7.

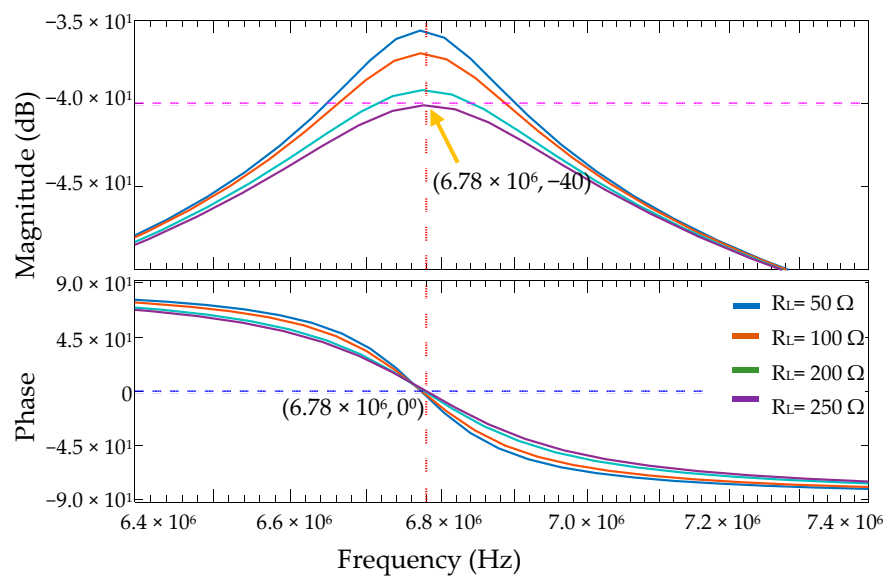


Figure 7. $|I_1/V_i|$ value in magnitude and phase.

The values of the parameters in asymmetrical S-CPT were calculated under resonance and match impedance conditions. The circuit must comply with both resonance and match impedance conditions to ensure the best performance of the system. Therefore, Equations (6) and (8) were used, and the graph shown in Figure 7 was plotted to calculate the inductor L_1 . The value of the load resistance, R_L , was adjusted from $50\ \Omega$ to $250\ \Omega$ to obtain the best fit at the 0° phase and $-40\ \text{dB}$ for the resonance condition and the match impedance condition, respectively. As shown in Figure 7, through a MATLAB simulation, the obtained load was determined to be $250\ \Omega$, and symmetrical S-CPT attained the resonance condition and match impedance at $6.78\ \text{MHz}$. Notably, when the load resistance is $250\ \Omega$, the magnitude value of $|I_1/V_i|$ approaches 0.01 , or $-40\ \text{dB}$, at $6.78\ \text{MHz}$ with 0° . Therefore, S-CPT works in maximum power transfer with a load resistance of $250\ \Omega$. In different applications with different loads, an additional matching impedance circuit is required to match the output of S-CPT to the application.

In the simulation, the symmetrical and asymmetrical topologies demonstrated a good agreement between the analysis and simulation results. It found that S-CPT can be formed into symmetrical and asymmetrical topologies. Therefore, the work proceeds with the asymmetrical S-CPT topology to investigate the hardware performance using the experimental setup.

In designing the asymmetrical S-CPT system, the coupler capacitance (C_c) and capacitance of the shield coupler (C_1 and C_2) were determined based on the coupler size; Table 3 lists the design values. The resistance load R_L at $250\ \Omega$ was selected as the calculated load obtained in the analysis.

Table 3. Parameters of S-CPT based on the design and measurement values.

Parameter	Symbol	Design Value	Hardware Value
Primary inductor top	$L_{P,top}$	$25.26\ \mu\text{H}$	$25.2\ \mu\text{H}$
Primary inductor bottom	$L_{P,bottom}$	$25.26\ \mu\text{H}$	$25.4\ \mu\text{H}$
Coupling capacitance top	$C_{CA,top}$	$10.0\ \text{pF}$	$10.02\ \text{pF}$
Coupling capacitance bottom	$C_{CA,bottom}$	$10.0\ \text{pF}$	$10.08\ \text{pF}$
Shield-coupling primary top	$C_{CP,top}$	$12.0\ \text{pF}$	$12.05\ \text{pF}$
Shield-coupling primary bottom	$C_{CP,bottom}$	$12.0\ \text{pF}$	$12.11\ \text{pF}$
Shield-coupling secondary top	$C_{S,top}$	$12.0\ \text{pF}$	$12.20\ \text{pF}$
Shield-coupling secondary bottom	$C_{S,bottom}$	$12.0\ \text{pF}$	$12.12\ \text{pF}$

Table 3 lists the design and measurement values of S-CPT, which are the calculated and hardware measurement values. The hardware value was determined by measuring the fabricated coupler. The parameters show a slight difference between the design value and hardware value owing to the fabrication process of the coupler and inductor.

2.1. Coupler Structure

A four-coupler structure with a shielding plate was designed and fabricated, as shown in Figure 8. Figure 8a shows the S-CPT system fabricated on a printed circuit board comprising FR4 material with a thickness of 1.6 mm. Figure 8b shows the shield plate and coupler plate arranged in parallel, using air as the dielectric. Figure 8c shows the dimensions of the coupler design. The gap between the couplers was adjusted to meet the design value, as shown earlier in Table 1; the measured hardware value indicates that the fabricated coupler has a tolerance of +3% from the design value.

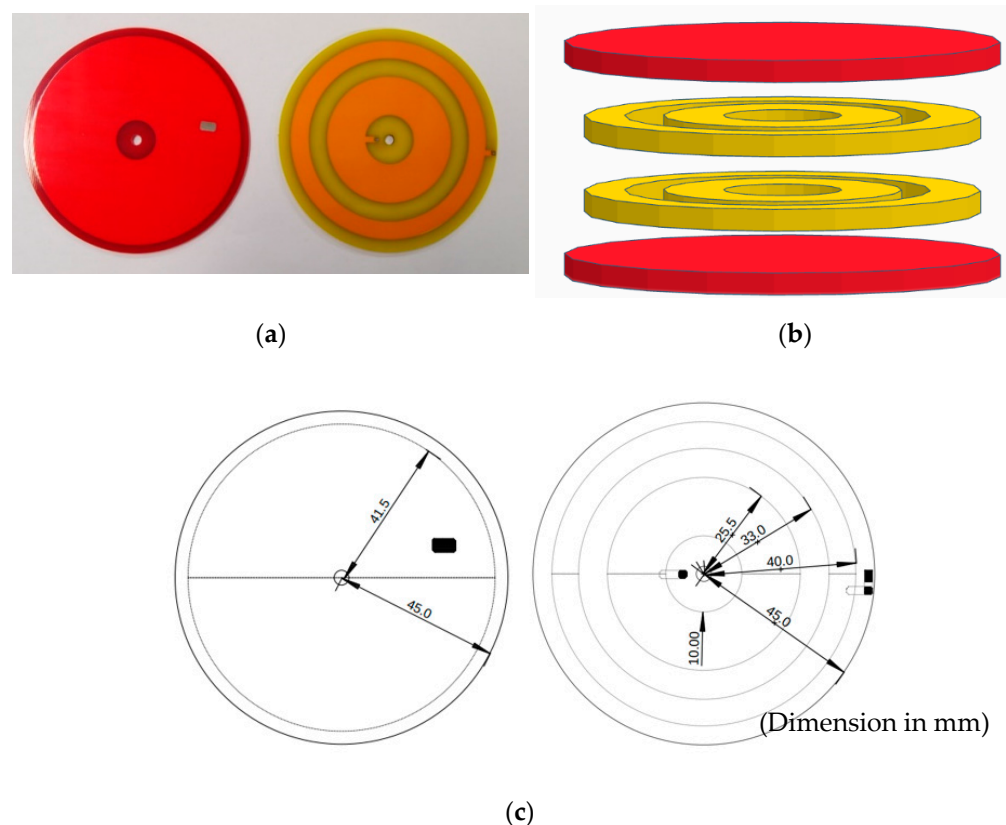


Figure 8. Four-coupler structure with a shielding plate. (a) Fabricated coupler hardware. (b) Coupler arrangement. (c) Two-dimensional (2D) drawing of the coupler structure.

Figure 9 illustrates the EF emission in the S-CPT coupler with the actual dimensions of the fabricated coupler, as shown earlier in Figure 8c, in which the gap between the shield plate and coupler is 1 mm, whilst the gap between the coupler and coupler is 2.5 mm. Quick Field software was used to simulate the EF emission with the actual fabricated dimensions and with the material properties between the plate and the air. The loading source and model class in the simulation was set to AC conduction and plane parallel, respectively. Furthermore, the frequency of 6.78 MHz was set with the measurement in mm value in the Cartesian coordinate system and the voltage at the coupler plate to 50 V for analysis purposes. Figure 9 shows the EF emissions.

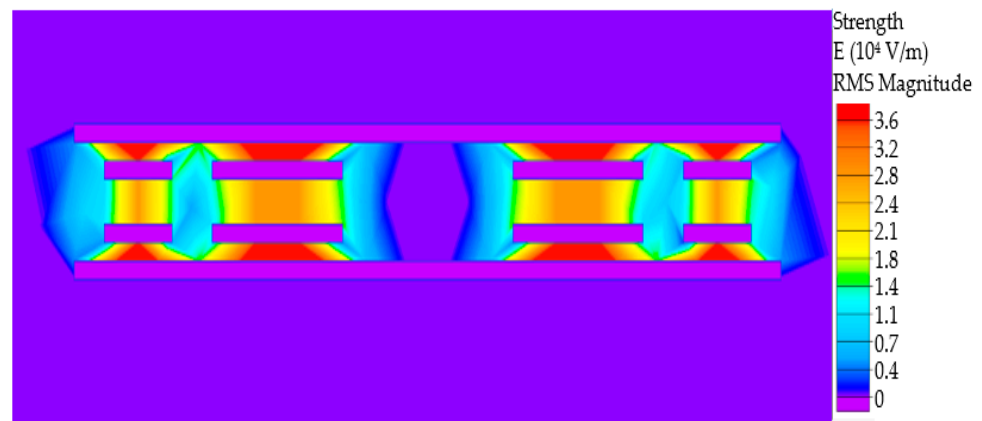


Figure 9. EF emission of S-CPT.

In Figure 9, the EF emission behind the shield plate is between 0 and 1 kV/m. EF emission occurs inside the coupler and at both the edges of the coupler. Based on the analysis result, the coupling and shield plates emit an EF with a maximum value of 35.4 kV/m, whereas the coupler-to-coupler has a maximum EF value of 28.3 kV/m. Moreover, an air breakdown voltage occurs when the EF reaches a limit value of 3000 kV/m or 30 kV/cm [19]. Therefore, the coupler design is under the breakdown voltage limit with a maximum EF emission of 35.4 kV/m. The simulated results also show that the shield plate in the S-CPT system minimises the EF reduction and acts as a safety feature in the system.

The International Commission on Non-Ionizing Radiation Protection (ICNIRP) guidelines set the exposure EF emission limit for humans to meet the safety requirements in designing S-CPT [22]. According to the ICNIRP guidelines, the EF emission with a 13.56 MHz frequency to the general public is 108.18 V/m and 48.48 V/m for 30 min and 6 min, respectively. Therefore, the EF emission was measured at the coupler edge to study the safety distance from the coupler. Figure 10 presents the data.

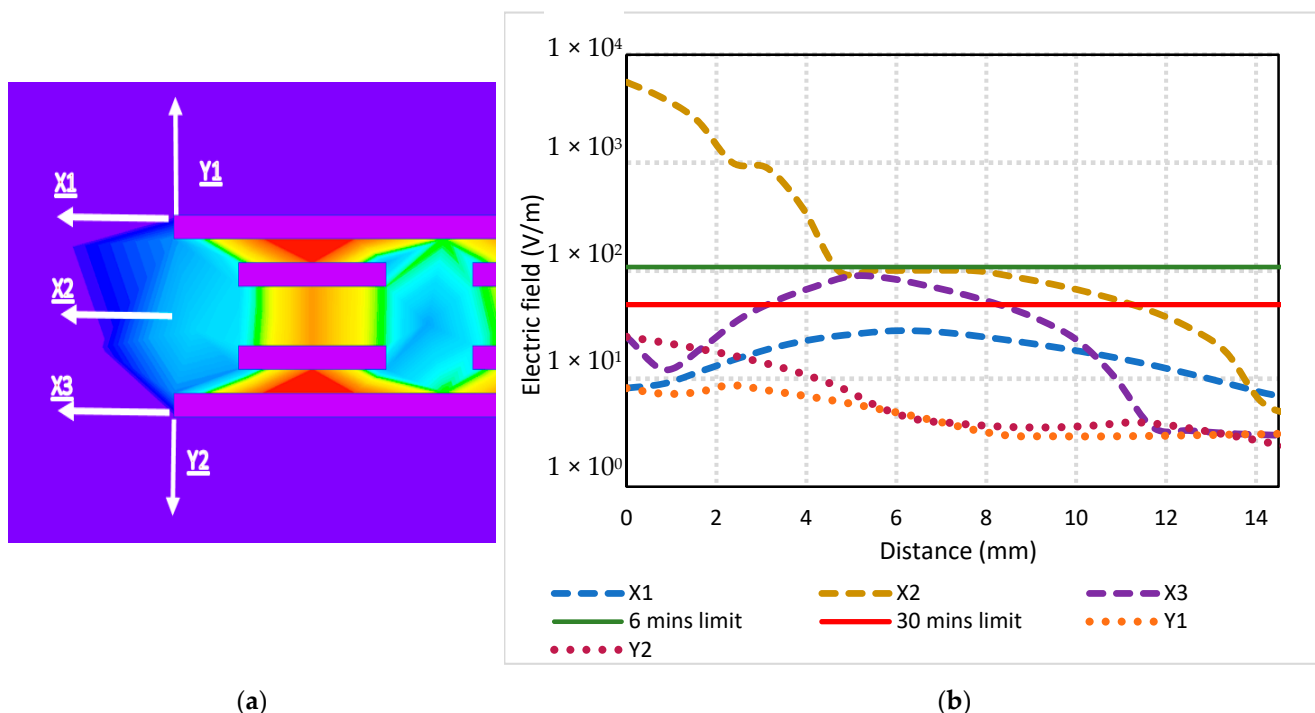


Figure 10. Emission field at the edge. (a) Measurement point at the edge (b) Emission field measurement result.

Figure 10 shows the electric emission at the edge of the S-CPT plates in which the measurement was performed on the x - and y -axes. The electric measurement was considered from 0 to 14.5 mm from the edge to study the electric field emission. Figure 10a shows the electric field emission measurement from the edge in the y -axis at the top shield point Y1 and bottom shield point Y2. Points X1, X2, and X3 show the measurement in the x -axis at the top shield and the centre point between the shield plate and bottom shield plate, respectively. Figure 10b shows the EF emission results at the edge, with the public exposure limit plotted at 108.18 V/m and 48.48 V/m in the graph. Notice in Figure 10b that the safe distance from EF emission is 12 mm from the coupler both at the x - and y -axes because the EF emission values from points X1, X2, X3, Y1, and Y2 are below the EF exposure limit. Y1 and Y2 indicate that the shield plate in S-CPT acts as a safety feature, with the EF emission values from 0 mm to 14.5 mm under both 108.18 V/m and 48.48 V/m. However, on the x -axis, the safe condition from EF exposure was 12 mm from the edge of the coupler.

Figure 11 shows the efficiency and impedance matching of the designed coupler and the fabricated hardware coupler. In terms of both efficiency and impedance matching, the fabricated hardware agrees with the designed coupler. Figure 11 indicates that the efficiency of the designed coupler is 1, whereas the hardware varies by 2%, which equals 0.98. The ideal value for the impedance matching of S-CPT is 0; however, the obtained design and hardware values are 0.03 and 0.13, respectively. Increasing the impedance matching value increases the reflected voltage through the primary side. Consequently, a high impedance matching value increases the loss. Therefore, good S-CPT designs have an impedance matching value close to 0.

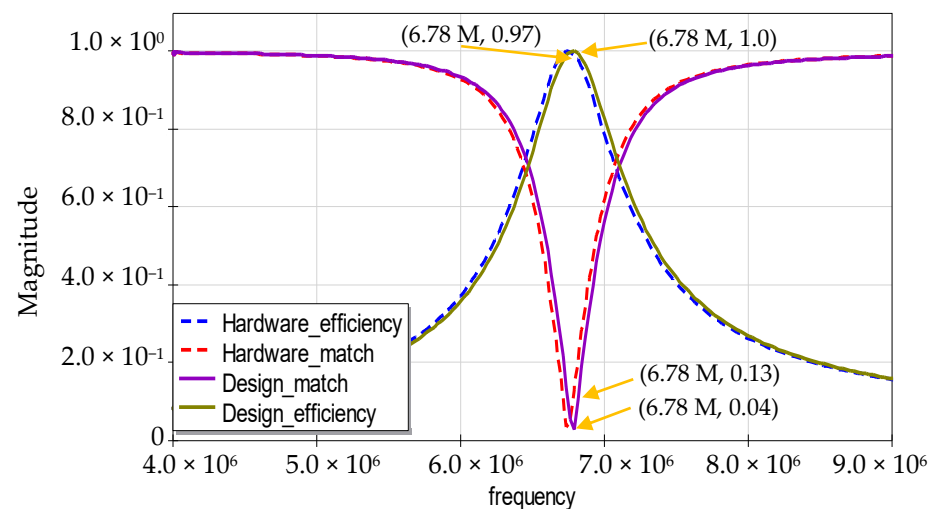


Figure 11. Efficiency and match impedance for the hardware and design value.

2.2. Class-E Inverter with a Balun

The class-E power amplifier in Figure 12 was designed with a 10-W S-CPT system, with an operating frequency of 6.78 MHz. Class E was designed using the equations [23]. Figure 12 presents the components of class E, whereas Table 4 lists the obtained parameters.

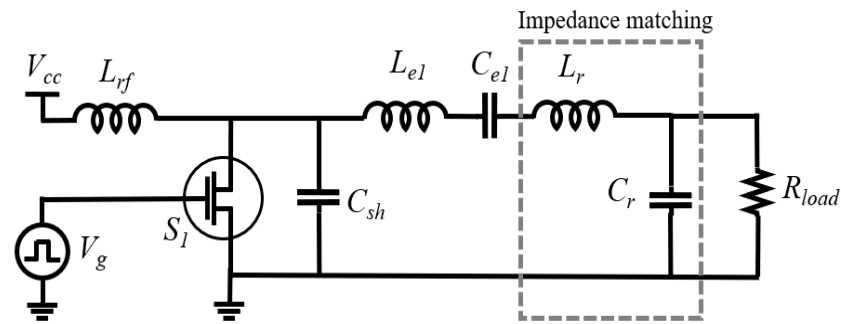


Figure 12. Class-E power inverter with an impedance matching circuit.

Table 4. Parameters of S-CPT based on the design and measurement values.

Parameter	Symbol	Design Value
Operating frequency	f	6.78 MHz
DC voltage	V_{cc}	12 V
Choke resistor	L_{rf}	3 μ H
Shunt Capacitor	C_{sh}	1.74 nF
Series inductor	$L_{e1} + L_r$	0.94 μ H
Series capacitor	C_{e1}	2.06 nF
Resonant capacitance	C_r	919 pF
Q value	Q_L	5
Load	R_{load}	50 Ω

The clock IC drives the voltage signal to the driver of the GanFET during the commuting process. Figure 13 shows the generated clock IC voltage and the output of the class-E inverter. The class-E inverter reached an efficiency of 79% with an output load of 50 Ω .

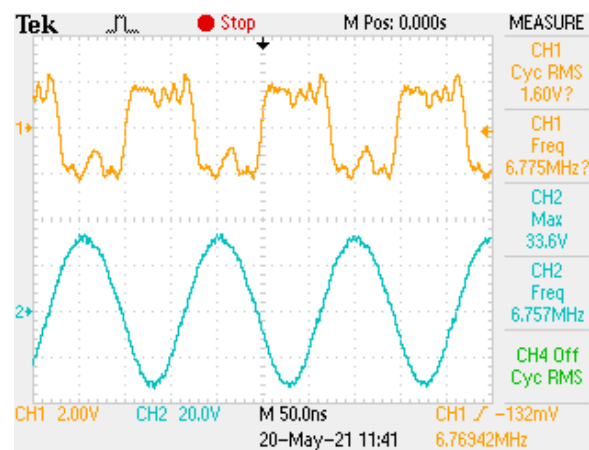
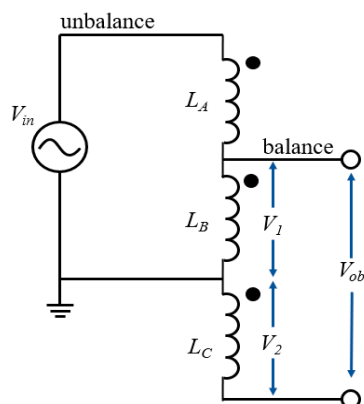


Figure 13. Clock voltage output and class-E voltage output.

A balun converts a single unbalanced signal into two balanced differential signals [24]. The Ruthroff-type balun has a lower insertion loss than a transformer type and requires ferrite as the core material to maintain its performance [25]. A narrow bandwidth moderates the insertion loss of the transformer type owing to its resonance mechanism [26]. Therefore, the S-CPT system used a Ruthroff 1:1 balun to convert the differential voltage, which was used as input for the CPT system. Figure 14 shows the Ruthroff balun

with two output voltages, and the relationship between the voltage outputs V_{ob} and output voltage is given in Equations (5) and (6).



(a)



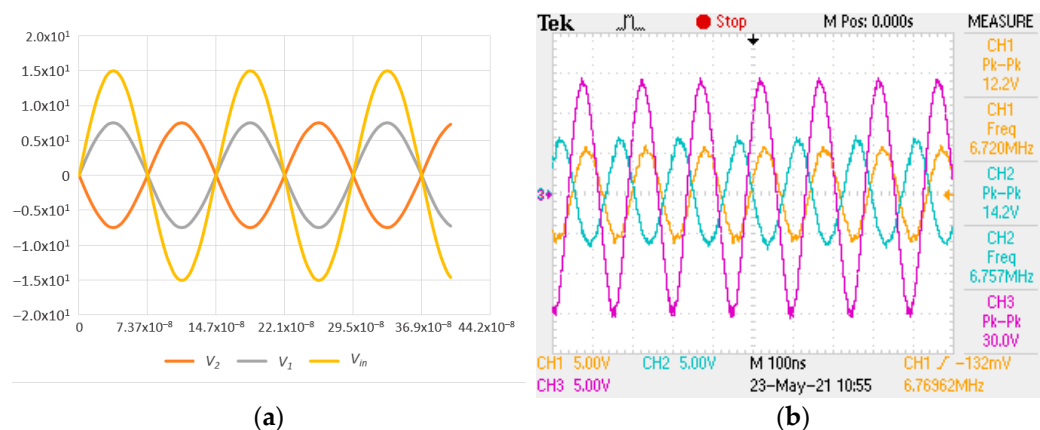
(b)

Figure 14. Ruthroff balun. (a) Circuit diagram. (b) Balun fabrication.

$$V_1 = \frac{V_{in}}{2} \quad (9)$$

$$V_{ob} = \frac{V_{in}}{2} - V_2 \quad (10)$$

The balun was analysed via both a simulation and an experiment, and Figure 15a,b presents the results, respectively. Figure 15a shows the simulated result of the balun with an input amplitude voltage of 15 V. Both the output voltages V_1 and V_2 exhibited an amplitude of 7.5 V. The experimental result in Figure 15b displays the input amplitude voltage of 15 V, in which the output voltages V_1 and V_2 were 6.1 and 7.1 V, respectively. These results show good agreement between the simulation and hardware values of the balun.



(a)

(b)

Figure 15. Voltage output and input of the balun. (a) Simulation. (b) Experiment.

The S-CPT system was set up as shown in Figure 16a,b to compare the voltage at the shield plate with and without the balun circuit. Figure 16a shows the connection of the components in the S-CPT system with class E, with the voltage points at the primary and secondary sides represented by GG_1 and GG_2 , respectively. The balun is connected to the inductor, and the complete topology is shown in Figure 16b with the voltage point at the shield plate in the primary part GD_1 and that in the secondary part GD_2 .

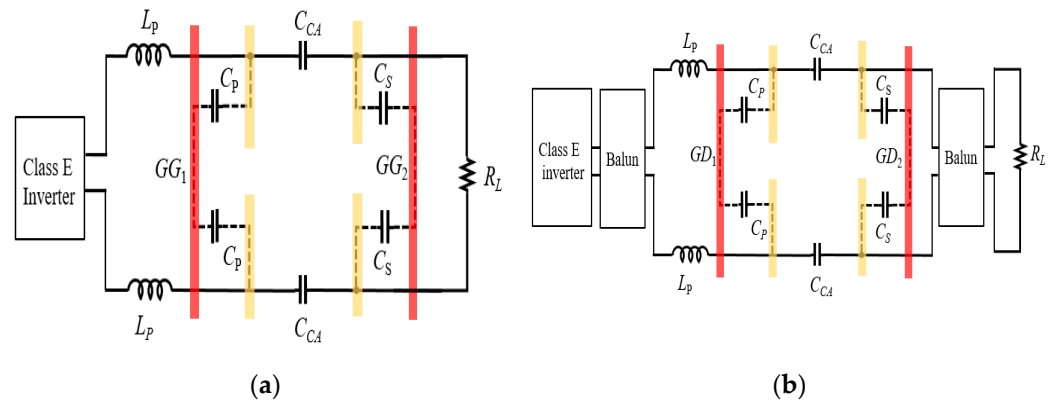


Figure 16. S-CPT system topology (a) without a balun and (b) with a balun.

Figure 17 shows the experimental setup with a balun. A Litz wire connects the balun to the air-core inductor. The coupler was fabricated and measured to meet the closest design value; Table 1 lists the measured values. The hardware experiment was set up to measure the voltage at the shield for S-CPT without and with the balun, as shown in Figure 16a,b, respectively.

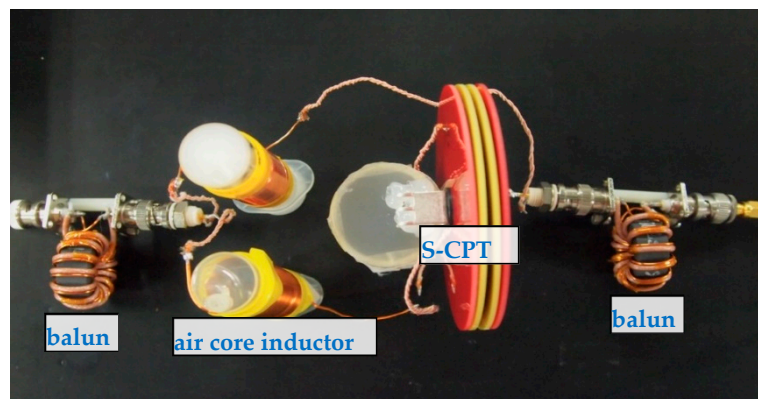
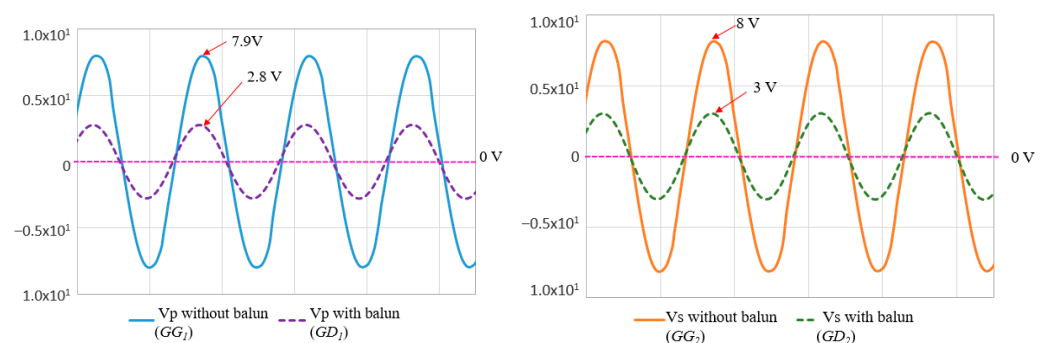


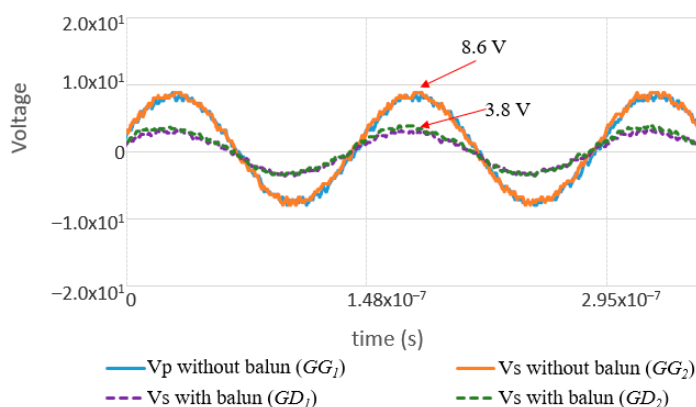
Figure 17. Experimental setup of the S-CPT system.

An LTspice simulation was used to investigate the voltage point in both circuits using a sinusoidal approach to observe and compare both topologies with the simulation results. Figure 18 shows the simulation and experimental results.



(a) Primary shield voltage (simulation).

(b) Secondary shield voltage (simulation).



(c) Primary and secondary shield voltage (experimental measurement).

Figure 18. Shield plate voltage. (a) Primary shield voltage in the simulation. (b) Secondary shield voltage in the simulation. (c) Shield voltage in the experiment.

3. Results and Discussion

Figure 18 shows the obtained simulation and experimental results for the voltage at the shield plate. A comparison was performed between the S-CPT system with and without a balun. The voltage input of both systems was 15 V in the amplitude value.

Figure 18 shows the simulated results for S-CPT with and without the balun at the primary and secondary sides, respectively. An ideal S-CPT system with a balun that has no internal resistance of the components and no unbalanced condition makes the voltage at the shield plate equal to zero. The balun produces two differential voltages at both S-CPT inputs, and the voltage becomes zero at the shield plate. Therefore, the S-CPT system becomes a grounding point and is safe for the shield plate. The design and measurement parameter values of S-CPT, as shown in Table 3, are simulated with a balun circuit, and the result shows the zero voltage at the shield plate, as plotted in Figure 18a,b. The measurement parameters of the fabricated S-CPT have voltages on both the primary and secondary sides, as shown in Figure 18a,b, owing to the unbalanced condition. Therefore, the ideal S-CPT system has zero voltage at the shield plate, with the difference in the fabricated component values contributing to the shield plate voltage.

Figure 18a illustrates that the voltage at the primary shield without the balun is 7.9 V in the amplitude value. Furthermore, the S-CPT system with the balun has a voltage of 2.8 V, which shows that the voltage at the shield plate of S-CPT without a balun is almost half of the input voltage of 15 V. Figure 18b shows that the secondary shield voltage with and without the balun generates amplitude voltages of 8 and 3 V, respectively. In comparison, the results in Figure 18a,b exhibit a reduction of 63% in the amplitude voltage in the S-CPT system with the balun. Therefore, the balun improves the ground stability by reducing the voltage at the shield plate.

Figure 18c shows the experimental results for both the primary and secondary shield plates with and without the balun. The results show that both the primary and secondary shield plates without a balun have an amplitude of 8.6 V. Furthermore, both the primary and secondary shield plates of the S-CPT balun reached an amplitude of 3.8 V. The experimental result of S-CPT with a balun demonstrated a reduction of 56% compared with S-CPT without a balun. Therefore, when the balun was used in the system, both the simulation and experimental results exhibited the same graph pattern and a 56% reduction in the voltage at the shield plate. Both the S-CPT system without balun and with a balun had an efficiency of 97.1% in the simulation value for transferring 7 W power. In the experiment, the system could transfer 7 W of power with an AC–AC efficiency of 84% and 80.5% for S-CPT without a balun and S-CPT with a balun, respectively. The reduction in the

efficiency of S-CPT with a balun shows that the balun may be lost owing to internal resistance and core loss.

The results show voltage at the shield plate in the S-CPT system without a balun, which makes the S-CPT system less safe. Therefore, the balun can reduce the voltage at the shield plate to improve ground stability and safety considerations.

4. Conclusions

An S-CPT system was developed with an operating frequency of 7 W by using a class-E power amplifier. The parameters in S-CPT were obtained using an analysis method in MATLAB simulation. A coupler was designed using four coupler plates with two shield plates. The simulated EF results show that the coupler can minimise EF emission. The S-CPT system was constructed, and the efficiency and impedance matching were measured. The results showed that the fabricated S-CPT was in good agreement with the simulation. The S-CPT system with class E was analysed with and without a balun circuit. The balun S-CPT showed a reduction of 56% in voltage at the shield plate compared with S-CPT without the balun. The hardware result validates the simulation results for S-CPT with and without a balun.

Author Contributions: Conceptualization and methodology, S.A., R.H., A.M. and T.M.M.; validation, S.A., A.M., and A.U.; hardware experiments, S.A. and A.U.; writing—original draft preparation, S.A. and A.U.; writing—review and editing, S.A., R.H., A.M. and A.U.; supervision, R.H., A.M., and T.M.M. All authors have read and agreed to the published version of the manuscript.

Funding: This research received no external funding.

Institutional Review Board Statement: Not applicable.

Informed Consent Statement: Not applicable.

Data Availability Statement: Not applicable.

Acknowledgments: The authors would like to thank members of Automotive System and Device Laboratories, Furukawa Electric Co., Ltd. through their technical support. Ministry of Higher Education (MOHE) Malaysia and Universiti Teknikal Malaysia Melaka through the SLAB scholarship support to S.A.

Conflicts of Interest: The authors declare no conflict of interest.

References

1. Lu, F.; Zhang, H.; Hofmann, H.; Mi, C. A CLLC-compensated high power and large air-gap capacitive power transfer system for electric vehicle charging applications. In Proceedings of the 2016 IEEE Applied Power Electronics Conference and Exposition (APEC), Long Beach, CA, USA, 20–24 March 2016; pp. 1721–1725, doi:10.1109/APEC.2016.7468099.
2. Sinha, S.; Regensburger, B.; Doubleday, K.; Kumar, A.; Pervaiz, S.; Afridi, K.K. High-power-transfer-density capacitive wireless power transfer system for electric vehicle charging. In Proceedings of the 2017 IEEE Energy Conversion Congress and Exposition (ECCE), Cincinnati, OH, USA, 1–5 October 2017; pp. 967–974, doi:10.1109/ECCE.2017.8095890.
3. Vu, V.B.; Dahidah, M.; Pickert, V.; Phan, V.T. An Improved LCL-L Compensation Topology for Capacitive Power Transfer in Electric Vehicle Charging. *IEEE Access* **2020**, *8*, 27757–27768, doi:10.1109/ACCESS.2020.2971961.
4. Muharam, A.; Mostafa, T.M.; Ahmad, S.; Masuda, M.; Obara, D.; Hattori, R.; Hapid, A. Preliminary study of 50 W Class-E GaN FET amplifier for 6.78 MHz capacitive wireless power transfer. *J. Mechatron. Electr. Power Veh. Technol.* **2020**, *11*, 22, doi:10.14203/j.mev.2020.v11.22-29.
5. Mostafa, T.M.; Muharam, A.; Hattori, R. Wireless battery charging system for drones via capacitive power transfer. In Proceedings of the 2017 IEEE PELS Workshop on Emerging Technologies: Wireless Power Transfer (WoW), Chongqing, China, 20–22 May 2017; doi:10.1109/WoW.2017.7959357.
6. Park, C.; Park, J.; Shin, Y.; Kim, J.; Huh, S.; Kim, D.; Park, S.; Ahn, S. Separated Circular Capacitive Coupler for Reducing Cross-Coupling Capacitance in Drone Wireless Power Transfer System. *IEEE Trans. Microw. Theory Technol.* **2020**, *68*, 3978–3985, doi:10.1109/TMTT.2020.2989118.
7. Yusop, Y.; Saat, S.; Ghani, Z.; Husin, H.; M.K, A.; Kiong Nguang, S. Cascaded Boost-Class-E for rotary capacitive power transfer system. *J. Eng.* **2019**, *2019*, 3742–3748, doi:10.1049/joe.2018.8016.

8. Ahmad, S.; Muharam, A.; Hattori, R. Rotary capacitive power transfer with class-E inverter and balun circuit. In Proceedings of the 2020 IEEE PELS Workshop on Emerging Technologies: Wireless Power Transfer (WoW), Seoul, Korea, 15–19 November 2020; pp. 330–333, doi:10.1109/WoW47795.2020.9291269.
9. Wu, X.; Su, Y.; Zou, L.J.; Member, S.; Liu, Z.H.E. A Sleeve-Type Capacitive Power Transfer System With Different Coupling Arrangements for Rotary Application. *IEEE Access* **2020**, *8*, 69148–69159, doi:10.1109/ACCESS.2020.2986359.
10. Dai, J.; Hagen, S.; Ludois, D.C.; Brown, I.P. Synchronous Generator Brushless Field Excitation and Voltage Regulation via Capacitive Coupling Through Journal Bearings. *IEEE Trans. Ind. Appl.* **2017**, *53*, 3317–3326, doi:10.1109/TIA.2017.2681621.
11. Yusop, Y.; Saat, S.; Nguang, S.K.; Husin, H.; Ghani, Z. Design of Capacitive Power Transfer Using a Class-E Resonant Inverter. *J. Power Electron.* **2016**, *16*, 1678–1688, doi:10.6113/jpe.2016.16.5.1678.
12. Sun, Y.; Yu, J.; Liu, X. Design of class-E power amplifier for capacitive power transfer system. *Microelectron. J.* **2018**, *80*, 69–74, doi:10.1016/j.mejo.2018.08.010.
13. Corti, F.; Reatti, A.; Wu, Y.-H.; Czarkowski, D.; Musumeci, S. Zero Voltage Switching Condition in Class-E Inverter for Capacitive Wireless Power Transfer Applications. *Energies* **2021**, *14*, 911, doi:10.3390/en14040911.
14. Zhang, H.; Lu, F.; Hofmann, H.; Liu, W.; Mi, C.C. A Four-Plate Compact Capacitive Coupler Design and LCL-Compensated Topology for Capacitive Power Transfer in Electric Vehicle Charging Application. *IEEE Trans. Power Electron.* **2016**, *31*, 8541–8551, doi:10.1109/TPEL.2016.2520963.
15. Zhu, Q.; Zou, L.J.; Su, M.; Hu, A.P. Four-plate capacitive power transfer system with different grounding connections. *Int. J. Electr. Power Energy Syst.* **2020**, *115*, 105494, doi:10.1016/j.ijepes.2019.105494.
16. Lu, F.; Zhang, H.; Hofmann, H.; Mi, C. A Double-Sided LCLC-Compensated Capacitive Power Transfer System for Electric Vehicle Charging. *IEEE Trans. Power Electron.* **2015**, *30*, 6011–6014, doi:10.1109/TPEL.2015.2446891.
17. Zhang, H.; Lu, F.; Hofmann, H.; Liu, W.; Mi, C.C. Six-Plate Capacitive Coupler to Reduce Electric Field Emission in Large Air-Gap Capacitive Power Transfer. *IEEE Trans. Power Electron.* **2018**, *33*, 665–675, doi:10.1109/TPEL.2017.2662583.
18. Muharam, A.; Ahmad, S.; Hattori, R.; Obara, D.; Masuda, M.; Ismail, K.; Hapid, A. An Improved Ground Stability in Shielded Capacitive Wireless Power Transfer. In Proceedings of the 2019 International Conference on Sustainable Energy Engineering and Application (ICSEEA), Tangerang, Indonesia, 23–24 October 2019; pp. 16–20, doi:10.1109/ICSEEA47812.2019.8938613.
19. Muharam, A.; Ahmad, S.; Hattori, R. Scaling-factor and design guidelines for shielded-capacitive power transfer. *Energies* **2020**, *13*, 4240, doi:10.3390/en13164240.
20. Ahmad, S.; Hattori, R.; Muharam, A. Generalized Circuit Model of Shielded Capacitive Power Transfer. *Energies* **2021**, *14*, 2826, doi:10.3390/en14102826.
21. Muharam, A.; Ahmad, S.; Hattori, R.; Hapid, A. 13.56 MHz scalable shielded-capacitive power transfer for electric vehicle wireless charging. In Proceedings of the 2020 IEEE PELS Workshop on Emerging Technologies: Wireless Power Transfer (WoW), Seoul, Korea, 15–19 November 2020; pp. 298–303, doi:10.1109/WoW47795.2020.9291299.
22. International Commission on Non-Ionizing Radiation Protection (ICNIRP). Guidelines for Limiting Exposure to Electromagnetic Fields (100 kHz to 300 GHz). *Health Phys.* **2020**, *105*, 483–524, doi:10.1097/HP.0000000000001210.
23. Sokal, B.N.O. Class-E RF Power Amplifiers. *Notes* **2001**, *204*, 9–20.
24. Li, E.S.; Lin, C.T.; Jin, H.; Chin, K.S. A broadband balun with complex impedance transformation and high isolation. *IEEE Access* **2019**, *7*, 112295–112303, doi:10.1109/ACCESS.2019.2934506.
25. Chung, H.; Chiou, H.; Hsu, Y.; Yang, T.; Chang, C. Design of Step-Down Broadband and Low-Loss Ruthroff-Type Baluns Using IPD Technology. *IEEE Trans. Compon. Packag. Manuf. Technol.* **2014**, *4*, 967–974, doi:10.1109/TCPMT.2014.2311662.
26. Chiou, H.K.; Chung, H.Y. Design of 9:4 step-down impedance transformation ruthroff balun with center tap in GIPD technology. In Proceedings of the 2018 IEEE CPMT Symposium Japan (ICSJ), Kyoto, Japan, 19–21 November 2018; Volume 2, pp. 193–196, doi:10.1109/ICSJ.2018.8602521.